Research Square

Preprints are preliminary reports that have not undergone peer review.
They should not be considered conclusive, used to inform clinical practice,
or referenced by the media as validated information.

# Fabrication of Ru-Ni/SBA-15 Bimetallic Catalyst: Synergistic Effect and Application in Linoleic Acid Isomerization

**Yigao Li**
Ministry of Education, Jiangnan University
**Shouteng Zheng**
Ministry of Education, Jiangnan University
**Pengpeng Huang**
Ministry of Education, Jiangnan University
**Xincheng Li**
Ministry of Education, Jiangnan University
**Mingming Fan**
fanmm2000@126.com
Ministry of Education, Jiangnan University
**Pingbo Zhang**
Ministry of Education, Jiangnan University

**Research Article**

**Keywords:** Linoleic acid, Conjugated linoleic acid, Isomerization, Bimetallic catalyst, Green catalysis

**Posted Date:** August 25th, 2026

**DOI:** https://doi.org/10.21203/rs.3.rs-10714314/v1

**License:** This work is licensed under a Creative Commons Attribution 4.0 International License.
Read Full License

**Additional Declarations:** No competing interests reported.

# Abstract

Aiming at green catalysis, an efficient and recyclable Ru-Ni/SBA 15 heterogeneous catalytic system was developed for the green isomerization of linoleic acid to prepare conjugated linoleic acid (CLA). Using P123 as a template agent and tetraethyl orthosilicate as the silicon source, an ordered mesoporous SBA-15 support was synthesized by the hydrothermal method, and a Ru-Ni bimetallic catalyst was prepared by the equal-volume co-impregnation method. Characterization using XRD, SEM, BET, XPS, and other techniques confirmed that the catalyst maintains an intact ordered 2D-hexagonal cylindrical mesoporous structure of SBA-15, whose large pore size and straight channels facilitate the diffusion of long-chain linoleic acid molecules. Ru and Ni highly dispersed and forming electronic synergistic effects, where Ru serves as the dominant active site to activate the C=C double bond of linoleic acid, while Ni modulates electron distribution and suppresses unwanted hydrogenation side reactions, significantly enhancing catalytic activity and stability. Under optimal conditions in an ethylene glycol system, the isomerization of linoleic acid catalyzed achieved a CLA yield of 65%. The catalyst can be separated and recovered by simple filtration, and it remains stably active after being reused four times. This system is simple to prepare, cost-controllable, and environmentally friendly, providing an efficient and feasible new route for the green synthesis of conjugated linoleic acid.


# 1 Introduction

Conjugated linoleic acid (CLA) is a general term for a class of naturally occurring positional and geometric isomers, which are derived from its parent compound—linoleic acid (cis-9,cis-12-octadecadienoic acid) through conjugated double bond derivatives.[1] Among the approximately 28 CLA isomers that have been identified, the cis-9, trans-11 and trans-10, cis-12 isomers have attracted considerable attention due to their outstanding biological activities.[2] A large number of studies have shown that CLA possesses a wide range of health-promoting effects, including but not limited to anti-cancer, anti-atherosclerosis, immune regulation, improvement of insulin sensitivity in type 2 diabetes, reduction of inflammatory responses.[3, 4] Therefore, relying on natural sources is far from sufficient to meet the growing market demand, and developing efficient and economical chemical synthesis methods to produce high-activity CLA isomers on a large scale has become a research focus.[5, 6] Currently, the methods for synthesizing CLA can be mainly divided into three categories: chemical catalytic isomerization, microbial enzymatic isomerization, and photochemical isomerization. Among these, the most commonly used method for industrial CLA production is base-catalyzed isomerization.[7] However, this approach has numerous inherent flaws: harsh reaction conditions, high energy consumption, equipment corrosion and waste liquid treatment issues, as well as the tendency for undesired trans, trans-conjugated isomers to form in the product.[8–10]

To overcome the limitations of homogeneous base-catalyzed methods, the development of recoverable and environmentally friendly heterogeneous catalysts has become a key development direction in the field of CLA synthesis.[11] Among numerous support materials, the mesoporous molecular sieve SBA-15

stands out for its unique structural properties. SBA-15 possesses a highly ordered two-dimensional hexagonal mesoporous structure (with tunable pore sizes of 4–30 nm), an ultrahigh specific surface area (> 800 $m^2/g$), a large pore volume, and relatively thick pore walls, endowing it with excellent thermal stability and hydrothermal stability.[12] The review by Verma and others systematically summarizes the latest trends and applications of SBA-15 in the field of catalysis, highlighting its flexibility in functional modification and active site design.[13] These characteristics not only facilitate the high dispersion and uniform distribution of active metal nanoparticles, preventing their aggregation, but also provide rapid diffusion pathways for reactant and product molecules, thereby effectively enhancing catalytic efficiency.[14] In addition, modifying the acidity or alkalinity of the SBA-15 support itself can also profoundly affect the catalytic performance.[15] The support retains its structural and morphological integrity after single-metal loading, while its catalytic performance is significantly enhanced.[16]

Although monometallic supported catalysts have demonstrated good catalytic performance, the balance between activity, selectivity, and cost still needs to be optimized.[17] Non-precious metals (such as Ni), although cost-effective, generally do not match precious metals in terms of activity, selectivity, and the ability to suppress side reactions.[18] In this context, constructing bimetallic catalysts has become an effective strategy to overcome the above bottlenecks. Bimetallic catalysts, through the 'synergistic effect' between two metals, can modulate the geometric structure and electronic properties of the active centers, producing unique 'alloyed' or 'intimately contacted' active phases.[19, 20] For example, Ni-based bimetallic/SBA-15 catalysts prepared by combining Ni with Cu, Mn or Zn exhibit superior deoxygenation activity and selectivity for target products in the hydrodeoxygenation of bio-oil compared to monometallic Ni catalysts.[21, 22] Chang and others reported a Ni/Rh dual-catalyst system, which, through Ni-catalyzed cross-coupling and Rh-catalyzed olefin isomerization tandem reactions, achieved the stereo convergent transformation of E/Z vinyl ether mixtures into highly E-selective allyl silanes.[23, 24] However, systematic studies on Ru-Ni bimetallic catalysts in linoleic acid isomerization reactions are currently lacking. The mechanisms of their synergistic effects, the optimal metal ratios, the influence of preparation methods on the structure of the active phase, as well as their regulation of catalytic activity, CLA yield, and the selectivity of target isomers, all remain to be thoroughly elucidated.[25, 26]

Based on this, the present study proposes using SBA-15 mesoporous molecular sieves as the support to prepare a series of Ru-Ni/SBA-15 bimetallic catalysts with different Ru/Ni molar ratios by the equal-volume co-impregnation method. By systematically adjusting the preparation process parameters and combining various characterization techniques, the study aims to deeply investigate the catalyst structure and metal-support interactions. Using linoleic acid isomerization as a model reaction, the catalytic activity, total CLA yield, and selectivity of each isomer under different reaction conditions will be thoroughly examined. By correlating the structural features of the catalysts with their catalytic performance, the essence of the Ru-Ni bimetallic synergistic effect will be elucidated, revealing the mechanism by which it regulates the reaction pathway of linoleic acid isomerization. This study aims to provide new design strategies and theoretical basis for the development of efficient, stable, and low-cost linoleic acid isomerization catalysts.

# 2 Experimental section

# 2.1 Experimental reagents and materials

Linoleic acid (LA), conjugated linoleic acid (CLA), poly (ethylene oxide)-poly(propylene oxide)-poly(ethylene oxide) triblock copolymer (P123), tetraethyl orthosilicate (TEOS), 1 mol/L hydrochloric acid, nickel nitrate hexahydrate ($Ni(NO_3)_2·6H_2O$), ruthenium(III) chloride trihydrate ($RuCl_3·3H_2O$)

# 2.2 Experimental method

**Synthesis of mesoporous SBA-15 carrier**

In this study, the preparation of SBA-15 mesoporous molecular sieves was carried out using a template-assisted hydrothermal synthesis method, with the triblock copolymer Pluronic P123 as a structure-directing agent and tetraethyl orthosilicate as the silicon source, self-assembling under acidic conditions; compared with the conventional method that removes the template by high-temperature calcination alone, the strategy adopted in this study, which combines extraction with low-temperature calcination, can more effectively preserve surface silanol groups.[27] At the same time, this method can significantly reduce pore structure shrinkage, maintaining the integrity of the carrier structure.[28] In addition, mild removal conditions help improve the loading stability of subsequent active components.[29]

The specific steps are as follows: Weigh 8 g of the template agent P123 and add it to a 250 mL beaker, then add 100 mL of 1.0 mol/L HCl solution. Mechanically stir at 40 ℃ until P123 is completely dissolved, forming a colorless transparent solution. Subsequently, add 16 g of TEOS dropwise, and continue stirring at this temperature for 12 h. Transfer the mixed solution into a 200 mL stainless steel autoclave lined with polytetrafluoroethylene, and allow it to crystallize undisturbed in a 100 ℃ oven for 24 h. After the reaction is complete, cool to room temperature, perform vacuum filtration, and wash repeatedly with deionized water. Dry the obtained white solid in a 100 ℃ oven overnight for 12 h, then grind to obtain a white powder. Under an air atmosphere, heat at a rate of 2 ℃/min to 550 ℃, and calcine in a muffle furnace for 4 h to obtain the SBA-15 sample. This synthetic route is based on the classical method proposed by Zhao Dongyuan and others,[30] Slight adjustments were made to the acid concentration and solvent ratio (HCl was adjusted to 1.0 mol/L, and the $H_2O$/TEOS molar ratio was reduced to 130), but the conditions remain strongly acidic and do not affect the formation of the ordered mesoporous structure.

**Preparation of monometallic and bimetallic catalysts**

Monometallic and bimetallic catalysts were prepared using the wet impregnation method. Nickel nitrate hexahydrate ($Ni(NO_3)_2·6H_2O$) and ruthenium trichloride trihydrate ($RuCl_3·3H_2O$) were used as the nickel and ruthenium sources, respectively. For the monometallic catalysts (nickel or ruthenium), the saturated water absorption of the support was determined in advance. According to the Ru (Ni) loading of 1% (10%), an appropriate amount of $RuCl_3·3H_2O$ ($Ni(NO_3)_2·6H_2O$) was weighed and dissolved in deionized

water to prepare the impregnation solution. The SBA-15 support was added to the impregnation solution, stirred at room temperature for 4 h, and then left to impregnate for 12 h. The impregnated sample was dried at 80 ℃ for 6 h, further dried at 100 ℃ for 2 h, and subsequently calcined in air at 550°C for 3 h. Finally, the sample was reduced in a hydrogen atmosphere at 350°C for 3 h ($H_2$ flow rate 50 mL/min), yielding the Ru/SBA-15 (Ni/SBA-15) catalysts. The reduced catalysts were cooled to room temperature under an inert atmosphere and stored sealed for further use. For the bimetallic catalysts (nickel and ruthenium), based on a Ni loading of 10% and Ru loading of 1%, appropriate amounts of $Ni(NO_3)_2 \cdot 6H_2O$ and $RuCl_3 \cdot 3H_2O$ were weighed and dissolved in deionized water, with the solution volume pre-determined according to the saturated water absorption of the support. The SBA-15 support was added to the above mixed solution, stirred at room temperature for 12 h and then allowed to impregnate for 12 h to ensure sufficient diffusion of metal ions into the mesoporous channels. The impregnated sample was dried at 100°C for 12 h, then calcined in air at 550°C for 4 h to decompose the metal precursors into NiO and $RuO_2$. Finally, the sample was reduced in a hydrogen ($H_2$) atmosphere at 350 ℃ for 3 h, producing the Ru-Ni/SBA-15 bimetallic catalyst.

## 2.3 Catalyst characterization

A scanning electron microscope (SEM) was used to observe the surface morphology and particle size distribution of the catalyst; an X-ray diffractometer (XRD) was employed to analyze the phase structure of the catalyst; an X-ray photoelectron spectrometer (XPS) was used to analyze the chemical states and relative contents of surface elements of the catalyst; a Fourier transform infrared spectrometer (FTIR) was used to characterize the surface functional groups of the catalyst; a fully automated specific surface area and porosity analyzer (BET) was employed to measure the specific surface area and pore structure parameters of the catalyst; a fully automated programmed temperature chemisorption analyzer was used to conduct $CO_2$-TPD and $NH_3$-TPD tests to characterize the surface acidity and basicity of the catalyst; a gas chromatograph (GC) was used for qualitative and quantitative analysis of the products.

# 3 Results and discussion

## 3.1 Structural and morphological characterizations

Table 1
Textural data of different catalysts

| Samples | Surface area ($m^2/g$) | Average pore diameter (nm) | Pore volume (cc/g) |
|---|---|---|---|
| SBA-15 | 1006.94 | 8.76 | 1.006 |
| Ru/SBA-15 | 373.82 | 2.43 | 0.524 |
| Ru-Ni/SBA-15 | 647.99 | 2.45 | 0.349 |
| Ru-Co/SBA-15 | 660.03 | 2.40 | 0.340 |

Small-angle XRD (Fig. 1a) was used to characterize the ordered pore structure of mesoporous materials: SBA-15 (black curve) shows distinct characteristic peaks at low angles (~ 1°), which are typical features of a two-dimensional hexagonally ordered mesoporous structure. Ru/SBA-15(red) and Ni/SBA-15(blue) still retain the characteristic peaks of SBA-15, indicating that after the loading of Ru and Ni, the mesoporous framework structure remains largely intact without obvious collapse, such well-ordered mesoporous channels are conducive to the diffusion of linoleic acid reactants and CLA products. Wide-angle XRD was used to identify crystal phase structures: Fig. 1b compares SBA-15, NiO/SBA-15, $RuO_2$/SBA-15, and $RuO_2$-NiO/SBA-15; SBA-15 shows no obvious crystalline peaks, indicating an amorphous support; NiO/SBA-15 shows characteristic peaks of NiO; $RuO_2$/SBA-15 and $RuO_2$-NiO/SBA-15 show characteristic peaks of $RuO_2$. Figure 1c compares SBA-15, Ru-Ni/SBA-15, Ru/SBA-15, and Ni/SBA-15. Characteristic peaks of metallic Ru and metallic Ni appear, indicating that the samples underwent reduction treatment and the metal oxides were reduced to the metallic state. The diffraction peaks of metallic Ni are significantly weakened, and only weak peaks of metallic Ru are detected over Ru-Ni/SBA-15, demonstrating that the co-loading of Ru and Ni improves the dispersion of bimetallic active sites on the SBA-15 support. All samples still retain the amorphous background of SBA-15, indicating that the support structure is stable.

Figure 1d-f show typical type IV isotherms, corresponding to the adsorption behavior of mesoporous materials. An H1-type hysteresis loop appears in the relative pressure range of P/P0 ≈ 0.4-1.0, which is a characteristic feature of ordered mesopores (such as the hexagonal channels of SBA-15). The three samples (d, e, f) all exhibit high adsorption amounts, indicating large specific surface areas and pore volumes and well-developed mesoporous structures. After metal loading, the adsorption slightly decreases because the metal particles occupy part of the pores or surface sites. The pore size distribution was calculated using the BJH method: Fig. 1g (corresponding to d) shows a maximum pore size of 11.01 nm with a narrow distribution, indicating uniform channels. Figure 1h (corresponding to e) shows a maximum pore size of 8.32 nm, slightly smaller, possibly due to partial filling of some channels after metal loading. Figure 1i (corresponding to f) shows a maximum pore size of 10.27 nm with a similarly narrow distribution, retaining the channel characteristics of the mesoporous material. Overall, the maximum pore sizes of the three samples are concentrated between 8 and 11 nm, within the typical mesoporous range, and the narrow distribution indicates that the channel structure of SBA-15 remains well-ordered after metal loading. Considering the kinetic diameters of linoleic acid (~ 0.80 nm) and conjugated linoleic acid (~ 0.75 nm), the mesoporous channels with sizes of 8–11 nm provide sufficient space for the free diffusion of reactants and products, enabling full contact between substrate molecules and highly dispersed Ru-Ni bimetallic active sites inside pores.

As shown in Table 1, after loading monometallic Ru, the specific surface area dropped sharply, from 1006.94 to 373.82 $m^2/g$, indicating that the high surface area mesoporous structure of the carrier was largely lost. The pore size and pore volume changed inversely: the pore size decreased sharply from 8.76 nm to 2.43 nm, while the pore volume dropped from 1.006 to 0.524 cc/g. The fundamental reason is that Ru species underwent severe agglomeration and sintering during high-temperature reduction/calcination, forming large particles that physically damaged the ordered pore walls of SBA-15.

The originally regular large mesopores were destroyed and converted into amorphous micropores/cracks, resulting in a significant decrease in specific surface area and average pore size. After loading Ru with Ni/Co bimetallic, the data followed a normal pattern, reflecting the synergistic effect of the bimetals. The structure remained stable, with the specific surface area moderately decreasing (approximately 60%-65% of the pure carrier), and the pore size remained around 2.4 nm, consistent with the pure carrier, and the pore size remained well-preserved. The underlying mechanism is that both Ni and Co can form strong metal-metal interactions with Ru, which effectively restrain the surface migration, agglomeration and sintering of Ru nanoparticles during thermal treatment. This confinement effect keeps Ru-based active sites highly dispersed, which only partially occupy the pore space and thus effectively protect the ordered mesoporous structure of SBA-15 from collapse.

Comprehensive conclusions can be drawn: the SBA-15 support has a stable structure, and after loading Ru, Ni (or their oxides), the mesoporous framework and ordered pore structure of SBA-15 remain basically intact, with no significant damage. The crystal phase is controllable; through reduction treatment, metal oxides ($RuO_2$, NiO) can be converted to their metallic states (Ru, Ni), and the corresponding characteristic peaks of these crystal phases can be clearly observed in XRD. The pore structure is uniform, and the samples retain the typical Type IV adsorption isotherms and narrow pore size distributions, with maximum pore diameters ranging from 8 to 11 nm, making them highly effective mesoporous catalytic materials. The effect of loading is minimal; metal loading reduces the specific surface area and pore volume and slightly decreases the pore size, but does not alter the mesoporous nature. Additionally, catalysts loaded with bimetals exhibit a more stable structure compared to those loaded with only Ru, which may be attributed to the synergistic effect between the two metals.

# 3.2 Surface morphology and element distribution

Analysis of the SEM morphology (Fig. 2a-f) shows that Fig. 2a (SBA-15) exhibits uniform micron-sized spherical particles (diameter approximately 2–5 μm) with smooth and rounded surfaces. This is characteristic of spray-dried SBA-15 mesoporous microspheres, reflecting the carrier's good spherical morphology and structural integrity. Figure 2b (Ru/SBA-15) indicates that after loading Ru, the spherical contour remains intact, but the surface becomes rough, with a large number of fine protruding particles corresponding to highly dispersed Ru metal nanoparticles, suggesting that the loading process did not damage the carrier framework and that the metal dispersion is good. Figure 2c (Ru-Ni/SBA-15) shows that after bimetallic loading, the spherical morphology remains stable, and the surface roughness further increases with denser fine particles, indicating that Ru and Ni are co-loaded and highly dispersed without significant aggregation. Figure 2d(low-magnification image) displays aggregated layered/folded particles with a size of about 10 μm, representing the bulk aggregated morphology of SBA-15 or its derived materials. Figure 2e(medium-magnification image) clearly displays ordered layers and mesoporous channel structures, resembling stacked two-dimensional hexagonal channels or layered silicate structures, reflecting a high specific surface area and abundant porosity. Figure 2f (high-magnification image) further enlarges the view, showing clearer pore outlines with uniform pore sizes,

indicating that the mesoporous structure of the carrier remains well-maintained after metal loading, providing efficient mass transfer channels and exposed active sites for catalytic reactions.

The distribution of elements and the energy spectrum (Fig. 2g-k) were analyzed. Based on the elemental mapping (Fig. 2g-j), the results were obtained: Fig. 2g (Si, yellow) shows that the Si element uniformly covers the entire spherical particle, corresponding to the $SiO_2$ framework of the SBA-15 support, demonstrating that the support structure is continuous and intact; Fig. 2h(O, blue) reveals that the distribution of O highly overlaps with that of Si, mainly originating from the Si–O bonds in $SiO_2$, while also including oxygen from the metal oxides, indicating that oxygen species are closely bound to the support framework; Fig. 2i (Ru, red) shows that the Ru element is uniformly dispersed on the surface of the spherical particles, with no obvious aggregation or large particles, confirming that Ru metal nanoparticles are highly dispersed on the support surface; Fig. 2j (Ni, green) presents the Ni element distribution completely overlapping with Ru, also uniformly dispersed, indicating that Ru and Ni achieve co-dispersion, which favors the formation of a bimetallic active interface and enhances catalytic performance. The EDS spectrum (Fig. 2k) clearly detects characteristic peaks of Si, O, Ni, and Ru, with no other impurity peaks, indicating high sample purity; the quantified elemental ratios (labeled) are approximately Si ~ 52%, O ~ 37%, Ni ~ 10%, and Ru ~ 1%, which closely match the designed loading (bimetallic Ru/Ni on SBA-15), validating the accuracy of the sample's chemical composition; the peak intensities of each element correspond to their atomic percentages, further confirming the proportion between the support and the metals.

The final conclusion is as follows: The catalyst exhibits stable morphology and structure. The spherical morphology and mesoporous channel structure of the SBA-15 support remain intact after loading Ru and Ni, with no collapse or deformation, demonstrating the structural stability of the support and its suitability for harsh catalytic reaction conditions. The metals are highly dispersed, where the co-existence of Ru and Ni realizes spatial confinement and mutual dispersion regulation: Ni effectively inhibits the migration and agglomeration of Ru nanoparticles during preparation, while highly dispersed Ru in turn anchors Ni species, achieving synergistic bimetallic dispersion. Ru and Ni bimetals achieve a high degree of uniform dispersion on the surface of the support without noticeable agglomeration, which is a key prerequisite for the catalyst to possess high activity, high selectivity, and stability. The composition is uniform, as evidenced by EDS mapping and energy-dispersive spectroscopy, which confirm the even distribution of Si, O, Ru, and Ni elements and that the chemical composition is consistent with the design, providing a structural basis for controllable regulation of catalytic performance. Such uniformly distributed Ru-Ni bimetallic interfaces created by spatial synergistic dispersion can provide abundant active sites for linoleic acid isomerization, laying a structural foundation for subsequent electronic synergy verified by XPS.

# 3.3 Acid and base site distribution

Fourier Transform Infrared Spectroscopy (FT-IR, Fig. 3a) shows that SBA-15 (red curve) fully retains all the characteristic framework peaks of mesoporous silica (1095, 810 $cm^{-1}$, etc.), while also exhibiting obvious peaks at 2935 and 1735 $cm^{-1}$, indicating that the template agent was not completely removed

and organic groups remain; the hydroxyl peak at 3440 $cm^{-1}$ is the most intense, corresponding to abundant Si-OH sites on the surface of the support. For Ru/SBA-15 (blue curve), the framework peaks (1095, 810 $cm^{-1}$) are fully retained, demonstrating that the mesoporous structure of SBA-15 was not destroyed after Ru loading; the intensity of the 3440 $cm^{-1}$ hydroxyl peak decreases significantly, indicating that Ru species interact with the Si-OH on the support surface (forming Ru-O-Si bonds), consuming hydroxyl groups; the template residual peaks at 2935 and 1735 $cm^{-1}$ have largely disappeared, showing that the loading process and subsequent calcination effectively removed the organic template. For Ru-Ni/SBA-15 (black curve), the framework peaks are also fully preserved, indicating that the co-loading of the two metals did not damage the support structure; the 3440 $cm^{-1}$ hydroxyl peak is further weakened, suggesting stronger interactions between the Ru and Ni bimetals and the support, with more Si-OH groups being consumed; no additional clear metal oxide characteristic peaks are observed (the characteristic peaks of $RuO_2$ and NiO are usually at low wavenumbers and weak, being overlapped by framework peaks), consistent with the behavior expected for low loading amounts.

According to the thermogravimetric analysis (TG, Fig. 3b) curve, SBA-15 (black curve) exhibits the least total weight loss (residual mass ~ 91% at 800 ℃), with weight loss occurring only due to the removal of adsorbed water and a small amount of hydroxyl condensation, without significant decomposition of organic residues, indicating that the template agent has been largely removed. The weight loss process is gradual, without obvious sharp weight loss steps, consistent with the thermal stability of pure mesoporous silica. Ru/SBA-15 (red curve) shows the greatest total weight loss (residual mass ~ 57% at 800°C), with a sharp weight loss step occurring between 200–400°C, corresponding to the decomposition and oxidation of Ru precursors (such as $RuCl_3$) and the combustion of residual organics; after 400 ℃, the weight loss tends to stabilize, indicating that the metal species have been fully converted to oxides, with improved thermal stability. Ru-Ni/SBA-15 (blue curve) has a total weight loss intermediate between the two (residual mass ~ 81% at 800 ℃), with a more gradual weight loss process, without the sharp steps observed in single-metal samples; the bimetallic precursors decompose stepwise, and the interaction between Ru and Ni suppresses excessive weight loss while maintaining the thermal stability of the support.

The curves obtained from the $CO_2$-TPD test (Fig. 3c) show that SBA-15 (black curve) exhibits almost no obvious $CO_2$ desorption peaks, indicating that the surface of pure mesoporous silica has almost no basic sites, consistent with the chemical properties of $SiO_2$. Ru/SBA-15 (red curve) shows prominent medium-to-high temperature desorption peaks at 600–800°C, indicating that after Ru loading, medium-strong basic sites are generated on the sample surface (originating from Ru–O–Si bonds and surface oxygen sites of Ru oxides); the peak area is moderate, corresponding to a limited number of basic sites. Ru-Ni/SBA-15 (blue curve) displays very strong desorption peaks at 500–700 ℃, with peak areas much larger than those of the monometallic samples, and the desorption temperatures slightly lower (mainly medium temperature); this indicates that after bimetallic loading, the number of basic sites on the sample surface increases significantly, with medium-to-strong basicity predominating, and the synergistic effect of Ru-Ni significantly enhances the abundance of basic sites. These enriched basic

sites can deprotonate the allylic C-H bond of linoleic acid to activate the substrate, while optimizing the local electronic microenvironment of Ru-Ni active centers to promote double-bond migration during isomerization.

According to the $NH_3$-TPD test (Fig. 3d), SBA-15 (black curve) exhibits only a weak low-temperature desorption peak around 100°C, corresponding to weak acidic sites on surface Si-OH groups, with no medium or high-temperature acidic sites, consistent with the weak acidity characteristics of pure $SiO_2$. Ru/SBA-15 (red curve) shows a low-temperature peak (~ 100°C) with intensity much higher than that of SBA-15, and a very weak medium-temperature peak around 200°C; this indicates that after Ru loading, the number of weak acidic sites significantly increases (new weak acidic sites are generated due to the interaction between Ru and Si-OH), while medium-strong acidic sites remain very few. Ru-Ni/SBA-15 (blue curve) exhibits a lower low-temperature peak intensity compared to the monometallic sample but shows multiple consecutive medium-to-high-temperature desorption peaks between 300–650°C with very large peak areas; this indicates that after bimetallic loading, the number of medium-strong/strong acidic sites is greatly enhanced, and the synergistic effect of Ru-Ni constructs abundant medium-strong to strong acidic sites on the support surface, with both acidity strength and site quantity far superior to those of the monometallic samples and the support. Medium-strong acidic sites can polarize the C = C double bond of linoleic acid to facilitate bond rearrangement, and the constructed acid-base synergistic microenvironment further regulates the adsorption-desorption behavior of substrates and products over bimetallic active sites.

# 3.4 Distribution of electronic valence states of elements

XPS is a core technique for surface chemical analysis, which identifies elemental composition, chemical bonding states, and atomic valence states by detecting photoelectron binding energy (Binding Energy, eV). The XPS survey spectrum of Ru/SBA − 15 (Fig. 4a) shows four distinct strong characteristic peaks on the binding energy axis, corresponding to C 1s (~ 284 eV), O 1s (~ 532 eV), Si 2p (~ 103 eV), and Ru 3d (~ 284 eV), directly confirming that the catalyst consists of three core elements: Ru, O, and Si. This is consistent with the material design of “Ru supported on SBA-15 carrier”, with no obvious impurity peaks and high elemental purity. After peak-fitting of the high-resolution O 1s spectrum of Ru/SBA − 15 (Fig. 4b), the spectrum is resolved into two characteristic peaks: the peak at ~ 536.0 eV (M-O peak, red) is assigned to metal-oxygen lattice bonds, corresponding to Ru-O or coordination bonds between the metal and the carrier, representing the key bonding form of catalytic active sites; the peak at ~ 530 eV (-OH peak, blue) is attributed to surface adsorbed hydroxyl groups (Si-OH and Ru-OH) or physically adsorbed water, reflecting the surface hydrophilicity of the material. It proves that both metal oxide active species and hydrophilic hydroxyl groups coexist on the catalyst surface, providing active sites and a surface microenvironment for the catalytic reaction. After peak-fitting of the high-resolution Si 2p spectrum of Ru/SBA − 15 (Fig. 4c), the peak at ~ 106 eV (Si-O-Si peak, red) represents the siloxane framework bond of the SBA-15 carrier, which is the core feature of the porous crystalline structure of the carrier; the peak at ~ 102.0 eV (Si-OH peak, blue) is assigned to terminal hydroxyl groups on the carrier surface, which not only reflects the integrity of the carrier but also provides anchoring sites for metal

loading. It verifies that the siloxane framework of the SBA-15 carrier is stable and retains active hydroxyl groups on the surface, supporting the strong metal-support interaction. In the high-resolution Ru 3d spectrum of Ru/SBA − 15 (Fig. 4d), the Ru 3d orbital exhibits doublet peaks ($3d_{5/2}$ and $3d_{3/2}$) due to spin-orbit splitting. Further deconvolution of valence states yields doublet peaks at ~ 284.0 eV and ~ 288.0 eV ($Ru^0$, red) corresponding to metallic ruthenium, which is an important active site for catalytic reactions; the peak at ~ 290.0 eV ($Ru^{4+}$, blue) corresponds to oxidized ruthenium, originating from the coordination of the metal with the carrier/oxygen, indicating the oxidation state of Ru. It confirms that Ru exists in a mixed valence state of $Ru^0$ and $Ru^{4+}$ in Ru/SBA − 15 with an approximate ratio of 12:1, and this valence distribution is crucial for regulating catalytic performance.

Compared with Fig. 4a, the XPS survey spectrum of Ru − Ni/SBA − 15 (Fig. 4e) presents an additional strong characteristic peak at ~ 855 eV corresponding to Ni 2p, while the peaks of O 1s, Si 2p, and Ru 3d remain visible. This directly proves that Ni is successfully introduced into the catalyst system, and the Ru-Ni bimetallic catalyst is prepared without other impurity elements. After peak-fitting of the high-resolution O 1s spectrum of Ru − Ni/SBA − 15 (Fig. 4f), the M-O peak (~ 528 eV) remains dominant, while the intensity of the -OH peak (~ 533 eV) decreases significantly. This indicates that after Ni doping, metal oxide species dominate the material surface and hydroxyl groups are reduced, demonstrating that Ni and Ru synergistically optimize the surface oxygen environment and enhance the metal-support interaction, which is more favorable for the catalytic reaction. The high-resolution Si 2p spectrum of Ru − Ni/SBA − 15 (Fig. 4g) still retains two characteristic peaks of Si-OH (~ 102.0 eV) and Si-O-Si (~ 99.0 eV), with peak positions and shapes basically consistent with those in Fig. 4c. This illustrates that Ni doping does not damage the siloxane framework of the SBA-15 carrier, and the porous structure and surface active sites of the carrier remain intact, ensuring the structural stability of the catalyst. The high-resolution Ru 3d spectrum of Ru − Ni/SBA − 15 (Fig. 4h) still shows the $Ru^0$ doublet (~ 282 eV, ~ 277 eV, red) and $Ru^{4+}$ characteristic peaks (~ 285 eV, ~ 278 eV, blue), but with slight shifts in peak positions and relative intensities. This confirms the electronic interaction between Ni and Ru (electron transfer from Ni to Ru), which slightly adjusts the valence state of Ru and reduces its binding energy, without changing the core coexistence state of $Ru^0$/$Ru^{4+}$ ($Ru^0$:$Ru^{4+}$ = 5:1). Such electronic synergistic effect is the key to improving catalytic performance. After peak-fitting of the high-resolution Ni 2p spectrum of Ru − Ni/SBA − 15 (Fig. 4i), the Ni 2p orbital is split into $2p_{3/2}$ and $2p_{1/2}$ peaks. Further deconvolution of valence states gives doublet peaks at ~ 870 eV and ~ 850.0 eV (red) corresponding to metallic $Ni^0$, the main active form of Ni in catalytic reactions; peaks at ~ 880 eV and ~ 860 eV (blue) correspond to the Ni $2p_{1/2}$ orbital, verifying that Ni exists in the + 2 oxidation state (NiO). It directly proves that both Ni active species and incompletely reduced NiO coexist in the catalyst with an approximate ratio of 1:1, forming a synergistic catalytic center with Ru active sites and significantly enhancing the catalytic performance of the material.

The composition of the catalyst is verified: Ru/SBA − 15 contains Ru, O, and Si; Ni is successfully introduced into Ru − Ni/SBA − 15 without any impurities, meeting the design requirements. The loading of Ru and Ni does not destroy the siloxane framework of the SBA-15 carrier, and the carrier structure

remains intact. The addition of Ni makes metal oxides dominant on the surface, increasing the number and quality of catalytic active sites and laying a structural foundation for improved catalytic performance. Ru always exists as $Ru^0/Ru^{4+}$, while Ni exists as $Ni^0/Ni^{2+}$. In the isomerization pathway, metallic Ruº serves as the primary active site to activate the C = C double bond of linoleic acid and drive double-bond migration, while high-valence $Ru^{4+}$ and $Ni^{2+}$ act as Lewis acidic sites to polarize allylic C–H bonds for substrate activation; metallic Niº further stabilizes the reaction intermediate and suppresses undesired hydrogenation side-reactions. The electronic interaction between Ni and Ru leads to electron transfer from Ni to Ru, where mixed-valent metal species construct an efficient electron-bridge channel, accelerating interfacial electron delivery and dynamic valence cycling between $Ru^0/Ru^{4+}$ and $Ni^0/Ni^{2+}$. This unique electronic synergy modulates the valence state of Ru and reduces its binding energy,, facilitating the adsorption of hydrogen atoms and the transfer of α-H, thereby improving the catalyst activity and promoting the isomerization of linoleic acid.

# 3.5 Catalytic activity tests

The carrier itself exhibits very low activity, with the conversion rate of pure SBA-15 being only ~ 5%, indicating that the carrier has no significant catalytic activity, and the activity originates from the supported metal components. Single-metal catalysts are less active than bimetallic ones; the conversion rates of Ni/SBA-15 and Ru/SBA-15 are approximately ~ 15% and ~ 47%, respectively, which are much lower than those of bimetallic catalysts. Ru-Ni/SBA-15 shows the best performance, with a conversion rate reaching 77% and a selectivity of 87%, making it the sample with the best overall performance; Ru-Co/SBA-15 has a conversion rate of ~ 57% and selectivity of ~ 80%, ranking second. There is a synergistic effect between the two metals, in this bimetallic system, metallic Ruº acts as the dominant active center to activate linoleic acid C = C bonds and drive double-bond migration for high conversion, while Niº modulates the local electronic environment of Ru active sites and suppresses undesired hydrogenation side-reactions to improve CLA selectivity. The geometric dispersion effect and interfacial electronic interaction between Ru and Ni jointly construct abundant bimetallic active sites, after co-loading Ru and Ni, both activity and selectivity are significantly higher than those of the single metals, demonstrating a synergistic catalytic effect that greatly enhances catalytic performance(Fig. 5a). The initial performance of the catalyst is excellent, with the conversion rate in the first cycle being ~ 77% and selectivity ~ 87%, consistent with the results in Fig. 5b; it exhibits good stability, with conversion and selectivity remaining essentially stable over the first three cycles. A slight decline occurs in the fourth and fifth cycles (with the fifth cycle showing a conversion of ~ 55% and selectivity of ~ 70%), but the performance remains relatively high. This catalyst is reusable, showing only minor deactivation after multiple cycles, meeting the practical requirements for heterogeneous catalysts and demonstrating potential for industrial applications.

Figure 5c ~ f respectively examine the effects of four key process parameters—solvent amount, reaction temperature, reaction time, and catalyst amount—on catalytic performance. The effect of solvent relative amount (0 ~ 16 mL/g) shows that the conversion rate rapidly increases with the increase of solvent amount, reaching a peak (~ 77%) at 8 mL/g, and then slightly decreases; the selectivity remains above

80% throughout, showing little influence from solvent amount. The optimal solvent amount is determined to be 8 mL/g, at which the conversion rate is highest and selectivity is stable. The effect of reaction temperature (160 ~ 200 ℃) shows that the conversion rate rapidly rises with increasing temperature, peaking (~ 77%) at 180 ℃; further increasing temperature (> 190 ℃) slightly reduces the conversion rate. The selectivity remains above 80% throughout, with a slight decrease at high temperatures. The optimal reaction temperature is determined to be 180 ℃; too low a temperature results in incomplete reaction, while too high a temperature may trigger side reactions leading to decreased selectivity. The effect of reaction time (3.0 ~ 5.0 h) shows that the conversion rate rapidly increases with prolonged time, peaking (~ 76%) at 4.0 h; further extending the time (> 4.5 h) results in a nearly constant conversion rate. The selectivity remains above 80% throughout, with minimal effect from reaction time. The optimal reaction time is determined to be 4.0 h, at which the reaction is basically complete, and further extension offers no significant benefit. The effect of catalyst relative amount (10%~50%) shows that the conversion rate rapidly increases with increasing catalyst amount, reaching a peak (~ 77%) at 30%; further increasing the amount (> 40%) maintains a nearly constant conversion rate. The selectivity remains above 80% throughout, with minimal impact from catalyst amount. The optimal catalyst amount is determined to be 30%, at which catalytic efficiency is highest, and excess catalyst provides no additional benefit but increases costs.

The experiment obtained the Ru-Ni/SBA-15 bimetallic catalyst with the optimal performance through screening, whose activity and selectivity are significantly superior to those of monometallic and other bimetallic systems. Stability tests demonstrated that this catalyst possesses good recyclability and can be reused multiple times. Through single-factor experimental process optimization, the optimal reaction conditions for this catalyst were determined: solvent-to-substrate ratio of 8 mL/g, reaction temperature of 180 ℃, reaction time of 4.0 h, and catalyst loading of 30%. Experimental validation showed that the catalyst has certain application value, achieving approximately 80% substrate conversion and over 85% target product selectivity under optimal conditions, providing an experimental basis for the industrial application of this catalytic reaction.

The introduction of Ni regulates the electronic and geometric structure of Ru active sites, forming a coupled bimetallic interface. This unique interface optimizes the adsorption and activation behavior of linoleic acid, effectively promoting allylic α-H abstraction and intermolecular hydrogen transfer, which is the core driving force for improved substrate conversion. Meanwhile, the bimetallic electronic interaction modulates the d-band center of active metals, weakening the excessive adsorption of active hydrogen on the catalyst surface and inhibiting undesirable full hydrogenation and random isomerization side reactions. Therefore, the Ru-Ni synergistic system precisely balances hydrogen activation efficiency and reaction pathway selectivity, realizing synchronous improvement in conversion efficiency and target CLA yield for linoleic acid isomerization.

# 4 Conclusion

This study aims at green catalysis and successfully constructs an efficient, recyclable, and environmentally friendly Ru-Ni/SBA-15 heterogeneous catalytic system, achieving the green and efficient isomerization of linoleic acid (LA) into high-value conjugated linoleic acid (CLA). This optimized Ru-Ni bimetallic system exhibits distinctive functional division and interfacial synergistic catalytic advantages for linoleic acid isomerization, fundamentally solving the defects of low activity and poor selectivity of single-metal Ru or Ni catalysts. In this reaction system, metallic $Ru^0$ serves as the core active site for catalytic isomerization, which can effectively activate the C = C double bonds of linoleic acid and promote the cleavage and migration of allylic α-H, thereby driving the progress of the isomerization reaction and guaranteeing high substrate conversion. By contrast, the introduced Ni species ($Ni^0$/$Ni^{2+}$) act as electronic modulators and selective regulators. The electron transfer from Ni to Ru optimizes the d-band center of Ru active sites, moderating the excessive adsorption and activation of active hydrogen on the catalyst surface. This effect effectively inhibits undesired side reactions such as full hydrogenation of double bonds and random disordered isomerization, thereby greatly improving the selectivity of target CLA products. Meanwhile, the Ru-Ni bimetallic interaction optimizes the surface acid-base microenvironment of the catalyst, further stabilizing the isomerization intermediates and reducing reaction energy barriers. Benefiting from the dual regulation of geometric dispersion and electronic synergy, the bimetallic catalyst realizes synchronous enhancement of catalytic activity and product selectivity, exhibiting excellent recyclability and stability. The catalyst can be quickly separated through simple filtration and retains high catalytic activity even after being reused four times, meeting the basic requirements for catalyst reuse in industrial applications. Moreover, the catalyst preparation process is straightforward, the reaction conditions are mild, and neither strong bases nor high temperature and high pressure are required, effectively avoiding the high pollution, high energy consumption, equipment corrosion, and excessive by-products associated with traditional base-catalyzed processes. This aligns with the principles of green chemistry and sustainable development.

This study elucidates the structure-activity relationship of Ru-Ni bimetallic synergistic promotion of linoleic acid isomerization, provides a reasonable explanation for the mechanisms of double bond migration and isomerization, offers experimental evidence and new ideas for the design of low-cost, highly active, and highly stable green catalysts for fatty acid isomerization, and also provides a practical and feasible technological pathway for the industrial green synthesis of conjugated linoleic acid.

## Declarations

# Conflict of interest

The authors declare no conflict of interest.

# Author Contribution

**Corresponding authors**

**Mingming Fan**: Writing – review & editing, Writing – original draft, Supervision, Resources, Project administration. **Pingbo Zhang**: Writing – review & editing, Resources, Project administration, Funding acquisition.

**Authors**

**Yigao Li**: Writing – review & editing, Writing – original draft, Methodology, Investigation, Formal analysis, Data curation, Conceptualization. **Shouteng Zheng**: Writing – review & editing, Writing – original draft, Methodology, Investigation, Formal analysis, Data curation, Conceptualization.

# Acknowledgments

This work was supported by the National Natural Science Foundation of China (No. 21978112) and MOE & SAFEA for the 111 Project (B13025) are gratefully acknowledged.

# Data availability

The data that support the findings of this study are available from the corresponding author on reasonable request.

## References

1. Fuke G, Nornberg JL (2017) Systematic evaluation on the effectiveness of conjugated linoleic acid in human health. Crit Rev Food Sci Nutr 57:1–7. https://doi.org/10.1080/10408398.2012.716800
2. Chorfa N, Hamoudi S, Belkacemi K (2010) Conjugated linoleic acid formation via heterogeneous hydrogenation/isomerization of safflower oil over mesostructured catalysts. Appl Catal A 387:75–86
3. Putera HD, Doewes RI, Shalaby MN et al (2023) The effect of conjugated linoleic acids on inflammation, oxidative stress, body composition and physical performance: a comprehensive review of putative molecular mechanisms. Nutr Metab (Lond) 20:35. https://doi.org/10.1186/s12986-023-00758-9
4. O'Shea M, Bassaganya-Riera J, Mohede IC (2004) Immunomodulatory properties of conjugated linoleic acid. Am J Clin Nutr 79. https://doi.org/10.1093/ajcn/79.6.1199S. :1199S-1206S
5. Zhang GM, Wen J, Chen JL et al (2007) Effect of conjugated linoleic acid on growth performances, carcase composition, plasma lipoprotein lipase activity and meat traits of chickens. Br Poult Sci 48:217–223
6. Lin L, Sun M-L, Wang K et al (2025) Biosynthesis of conjugated linoleic acid: current status and future perspectives. Bioresour Bioprocess 12:72

7. Kyselka J, Thomes L, Remišová S et al (2016) Preparation of conjugated linoleic acid enriched derivatives by conventional and biphasic isomerisation. Czech J Food Sci 34:511–521. https://doi.org/10.17221/362/2016-CJFS
8. Andjelkovic DD, Min B, Ahn D, Larock RC (2006) Elucidation of Structural Isomers from the Homogeneous Rhodium-Catalyzed Isomerization of Vegetable Oils. J Agric Food Chem 54:9535–9543. https://doi.org/10.1021/jf0612124
9. Pakdeechanuan P, Intarapichet K-O, Fernando LN, Grün IU (2005) Effects of Rhodium Heterogeneous Catalyst and Isomerization Conditions on Linoleic Acid Conjugation of Soybean Oil. J Agric Food Chem 53:923–927
10. Bernas A, Kumar N, Mäki-Arvela P et al (2004) Heterogeneous Catalytic Production of Conjugated Linoleic Acid. Org Process Res Dev 8:341–352
11. Chorfa N, Hamoudi S, Arul J, Belkacemi K (2013) Sulfur Promotion in Conjugated Isomerization of Safflower Oil over Bifunctional Structured Rh/SBA-15 Catalysts. ChemCatChem 5:1917–1934. https://doi.org/10.1002/cctc.201200895
12. Du J, Kuang W, Xu H et al (2008) The influence of precursors on Rh/SBA-15 catalysts for $N_2O$ decomposition. Appl Catal B 84:490–496. https://doi.org/10.1016/j.apcatb.2008.05.004
13. Verma P, Kuwahara Y, Mori K et al (2020) Functionalized mesoporous SBA-15 silica: recent trends and catalytic applications. Nanoscale 12:11333–11363
14. Perumal SK, Lee S, Yu H et al (2024) Synergistic Interaction between Ruthenium Catalysts and Grafted Niobium on SBA-15 for 2,5-Furandicarboxylic Acid Production Using 5-Hydroxymethylfurfural. ACS Appl Mater Interfaces 16:7353–7363. https://doi.org/10.1021/acsami.3c18720
15. Jambhulkar DK, Ugwekar RP, Bhanvase BA, Barai DP (2022) A review on solid base heterogeneous catalysts: preparation, characterization and applications. Chem Eng Commun 209:433–484
16. Chen J, Zhang L, Zheng X, Zheng Y (2017) Revealing ruthenium and basicity synergetic effects in Ru–MgAl catalysts for isomerization of linoleic acid to conjugated linoleic acid. RSC Adv 7:54747–54755
17. Kemache N, Hamoudi S, Arul J, Belkacemi K (2010) Activity and Selectivity of Nanostructured Sulfur-Doped Pd/SBA-15 Catalyst for Vegetable Oil Hardening. Ind Eng Chem Res 49:971–979. https://doi.org/10.1021/ie9006529
18. Mukesh D, Narasimhan CS, Deshpande VM, Ramnarayan K (1988) Isomerization of methyl linoleate on supported ruthenium-nickel catalyst. Ind Eng Chem Res 27:409–414. https://doi.org/10.1021/ie00075a008
19. Erdogan B, Arbag H, Yasyerli N (2018) SBA-15 supported mesoporous Ni and Co catalysts with high coke resistance for dry reforming of methane. Int J Hydrog Energy 43:1396–1405
20. Oh S, Lee JH, Choi I-G, Choi JW (2020) Enhancement of bio-oil hydrodeoxygenation activity over Ni-based bimetallic catalysts supported on SBA-15. Renewable Energy 149:1–10

21. Bernas A, Mäki-Arvela P, Kumar N et al (2003) Heterogeneously Catalytic Isomerization of Linoleic Acid over Supported Ruthenium Catalysts for Production of Anticarcinogenic Food Constituents. Ind Eng Chem Res 42:718–727. https://doi.org/10.1021/ie020642q
22. Guo Y, Wei Z, Zhang Y, Cao J (2024) The Effects of *trans* – 10, *cis* – 12 Conjugated Linoleic Acid on the Production Performance of Dairy Cows and the Expression and Transcription Regulation of Lipid Metabolism-Related Genes in Bovine Mammary Epithelial Cells. ACS Omega 9:34161–34174
23. Bergamo P, Luongo D, Miyamoto J et al (2014) Immunomodulatory activity of a gut microbial metabolite of dietary linoleic acid, 10-hydroxy-cis-12-octadecenoic acid, associated with improved antioxidant/detoxifying defences. J Funct Foods 11:192–202. https://doi.org/10.1016/j.jff.2014.10.007
24. Chang Y-C, Yang H-L, Chou Y-Y et al (2026) Sequential Ni-Catalyzed Cross-Coupling and Ru-Catalyzed Isomerization of *E* / *Z* Alkenyl Ethers: A Stereoconvergent Route to Allylsilanes. J Org Chem 91:761–766
25. Kumari Ramiah S, Meng GY, Ebrahimi M (2014) Dietary Conjugated Linoleic Acid Alters Oxidative Stability and Alleviates Plasma Cholesterol Content in Meat of Broiler Chickens. Sci World J 2014:1–10
26. Philippaerts A, Goossens S, Vermandel W et al (2011) Design of Ru–Zeolites for Hydrogen-Free Production of Conjugated Linoleic Acids. Chemsuschem 4:757–767. https://doi.org/10.1002/cssc.201100015
27. Khalilzadeh A, Shariati A (2019) Photoconversion of $CO_2$ over Fe-N-Ti@xSBA nanocomposite to produce hydrocarbon fuels. J $CO_2$ Utilization 33:21–30. https://doi.org/10.1016/j.jcou.2019.05.007
28. de Ávila SG, Silva LCC, Matos JR (2016) Optimisation of SBA-15 properties using Soxhlet solvent extraction for template removal. Microporous Mesoporous Mater 234:277–286
29. Jia J, Liu X, Wu K et al (2019) Loading zedoary oil into pH-sensitive chitosan grafted mesoporous silica nanoparticles via gate-penetration by supercritical $CO_2$ (GPS). J $CO_2$ Utilization 33:12–20
30. Zhao D, Feng J, Huo Q et al (1998) Triblock Copolymer Syntheses of Mesoporous Silica with Periodic 50 to 300 Angstrom Pores. Science 279:548–552

## Scheme

Scheme 1 is available in the Supplementary Files section.

## Figures

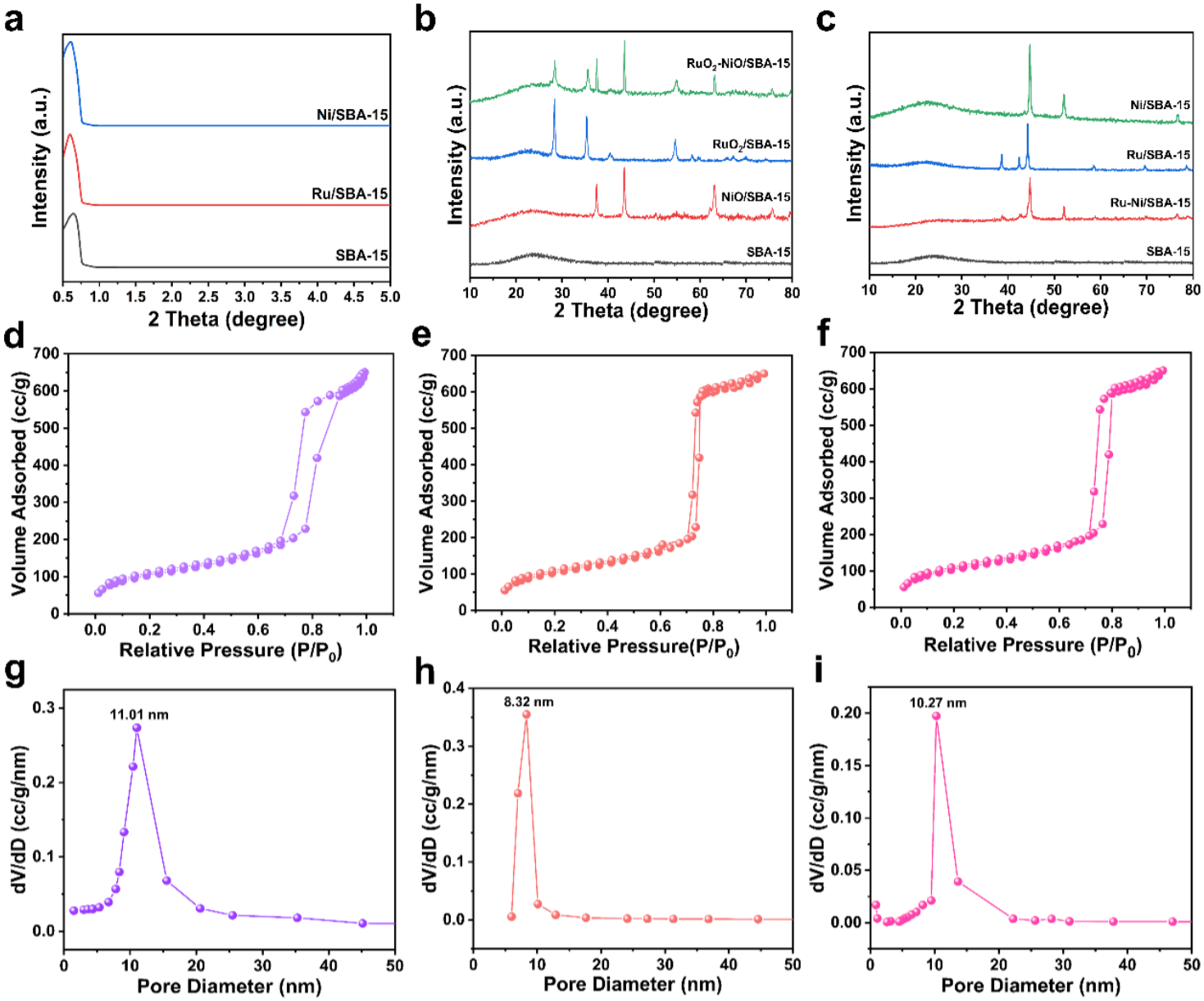


**Figure 1**

XRD patterns of the catalysts: (a) small-angle, (b) before reduction, (c) after reduction; (d) SBA-15, (e) Ru/SBA-15, (f) Ru-Ni/SBA-15 $N_2$ adsorption-desorption isotherms; (g) SBA-15, (h) Ru/SBA-15, (i) Ru-Ni/SBA-15 pore size distributions

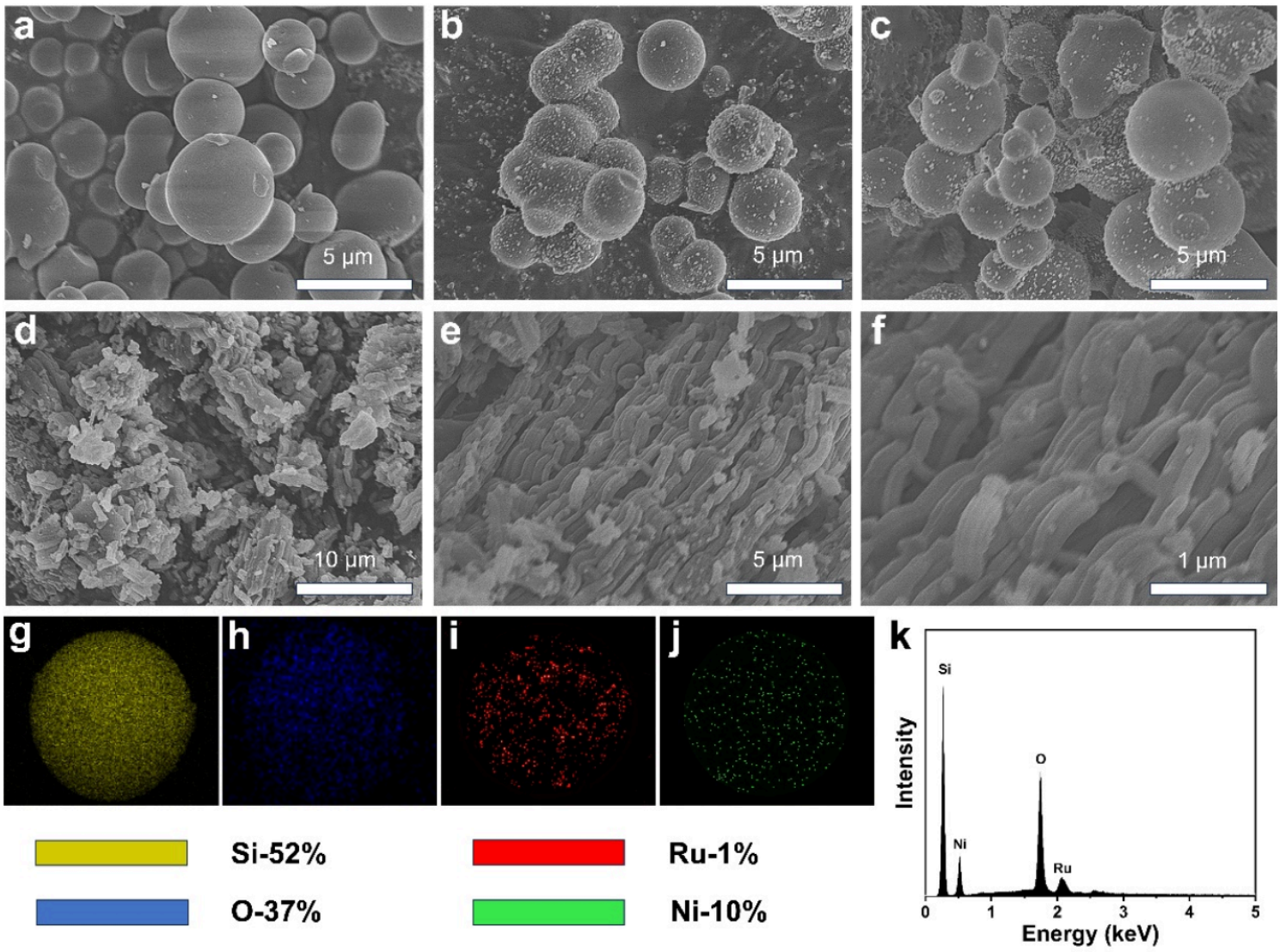


**Figure 2**

(a) SEM image of SBA-15, (b) Ru/SBA-15, (c) Ru-Ni/SBA-15; (d–f) SEM images of the catalyst at different magnifications; (g–j) EDS images of Ru-Ni/SBA-15; (k) EDS spectrum of Ru-Ni/SBA-15

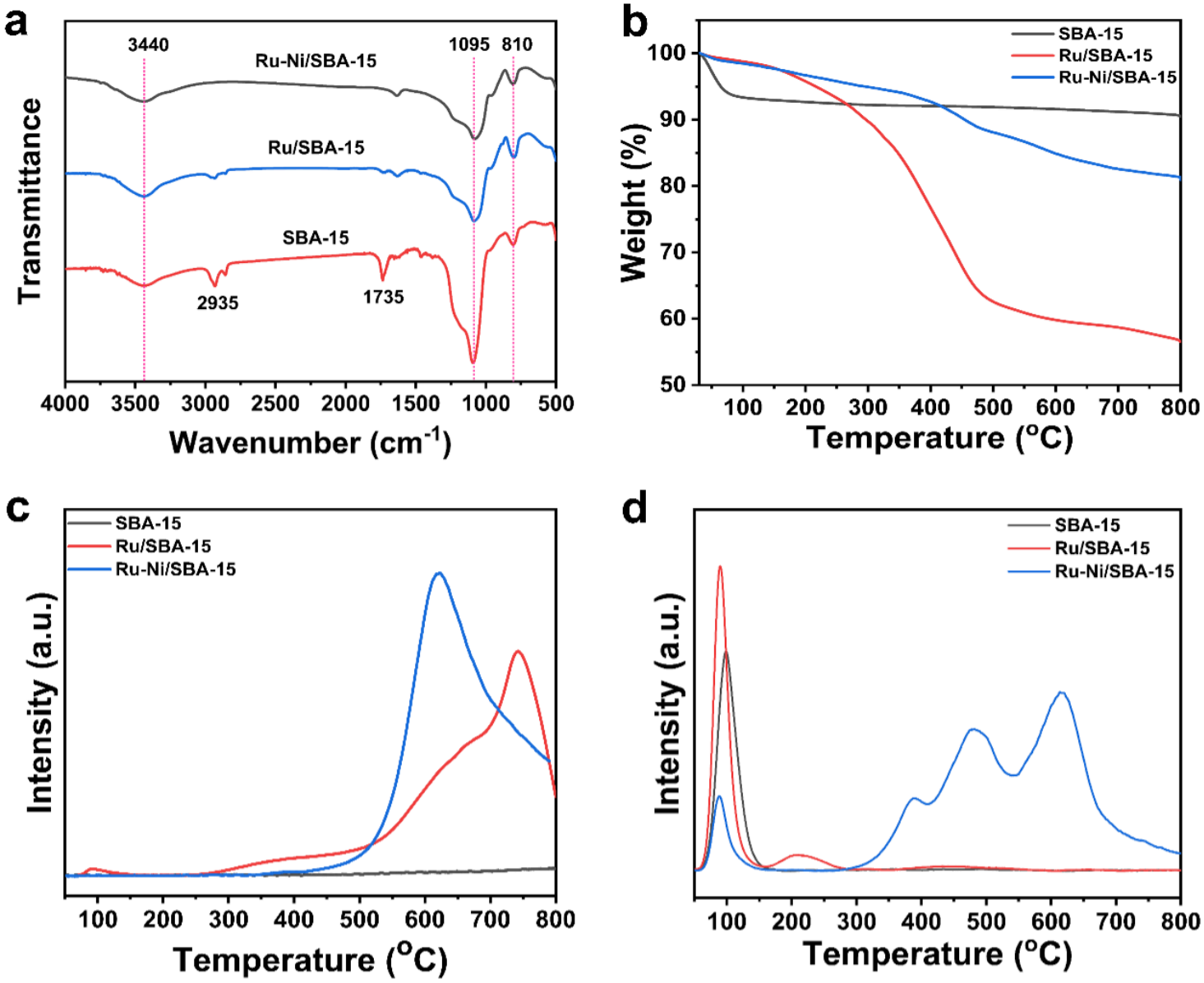


**Figure 3**

(a) Fourier Transform Infrared Spectra (FT-IR), (b) Thermogravimetric Analysis (TG), (c) $CO_2$-TPD, and (d) $NH_3$-TPD tests of SBA-15, Ru/SBA-15, and Ru-Ni/SBA-15

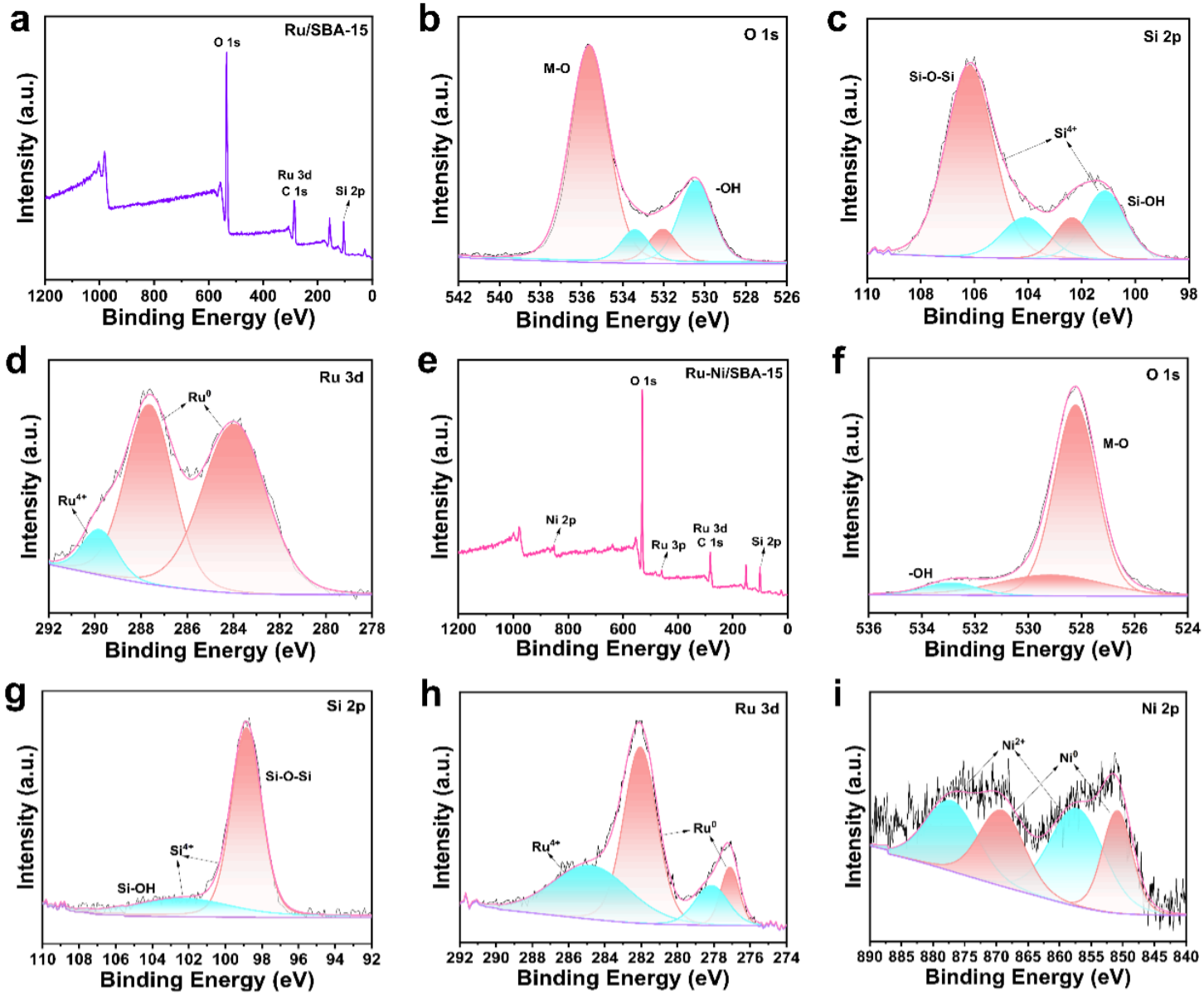


**Figure 4**

(a) XPS survey spectrum of Ru/SBA-15, (b) O 1s, (c) Si 2p, (d) Ru 3d high-resolution XPS spectra; (e) XPS survey spectrum of Ru-Ni/SBA-15, (f) O 1s, (g) Si 2p, (h) Ru 3d, (i) Ni 2p high-resolution XPS spectra

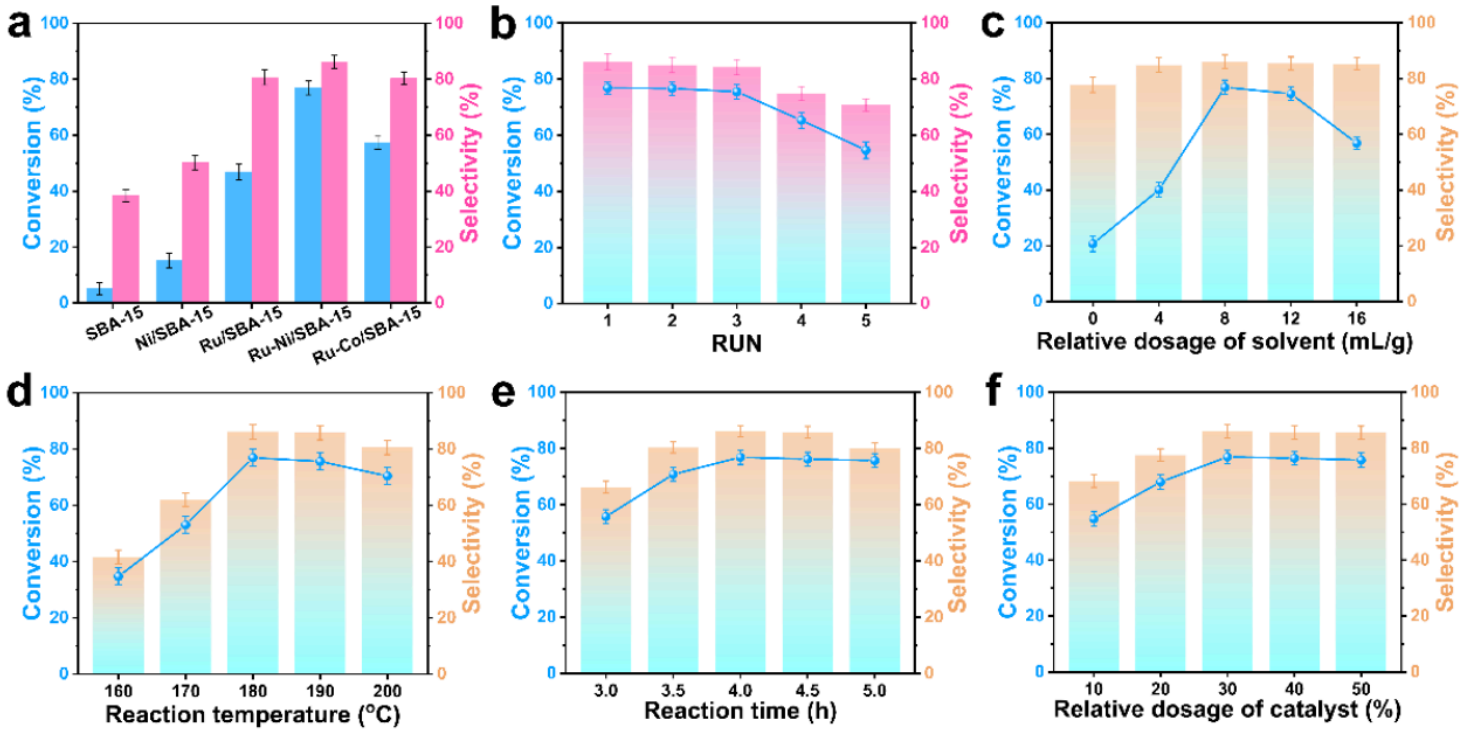


**Figure 5**

(a) Comparison of the activities of different catalysts; (b) Reusability test of the catalyst Ru-Ni/SBA-15; (c~f) Effects of Ru-Ni/SBA-15 on the reaction under different conditions

## Supplementary Files

This is a list of supplementary files associated with this preprint. Click to download.

- GraphicalAbstract.docx
- Scheme1.docx